IEEE Access
Multidisciplinary ⋮ Rapid Review ⋮ Open Access Journal

Received July 21, 2021, accepted August 12, 2021, date of publication August 16, 2021, date of current version August 24, 2021.

Digital Object Identifier 10.1109/ACCESS.2021.3105194

Theory of Resonant Modes and Its Application

RUQI XIAO[1], WEN GEYI[2], (Fellow, IEEE), AND WEN WU[1], (Senior Member, IEEE)
[1]Ministerial Key Laboratory of JGMT, Nanjing University of Science and Technology, Nanjing 210094, China
[2]Research Center of Applied Electromagnetics, Nanjing University of Information Science and Technology, Nanjing 210044, China

Corresponding author: Ruqi Xiao (Xiaoruqi_ee@njust.edu.cn)

This work was supported by the Chinese Natural Science Foundation under Grant 61971231.

ABSTRACT This paper proposes a unified procedure for evaluating the resonant frequencies and the corresponding resonant modes for an arbitrary source region, based on the general expression for the difference between the stored magnetic and electric field energies in terms of the source current distribution. It is shown that the resonant frequencies and the corresponding resonant modes are governed by a homogeneous integral equation. By following a standard procedure of the method of moments (MoM), the integral equation can be discretized into a real homogenous algebraic equation, from which the resonant frequencies and the corresponding resonant modes can be determined by requiring that a non-trivial solution exists for the real homogeneous algebraic equation. Different from other modal theories that expand the fields by a linear combination of fundamental field patterns that are derived from the boundary conditions, the proposed theory of resonant modes is derived from the difference of stored field energies for an arbitrary source region. As an application of the theory of the resonant modes, a crossed-dipole antenna, a dual-band bowtie antenna, and a dual-band circular polarization antenna are designed through the appropriate excitations of the resonant modes on the three selected source regions, and they are validated by independent simulations and experiments.

INDEX TERMS Theory of resonant modes, stored electromagnetic field energy, crossed-dipole antenna, bowtie antenna, dual-band circular polarization antenna.

I. INTRODUCTION

The modal theory for a scatterer plays an important role in antenna theory and designs. The basic idea behind the modal theory is to introduce a number of fundamental field patterns, called modes, so that the fields outside the scatterer can be expanded into a linear combination of these modes [1]. The modal theory becomes extremely useful wherever the linear combination is dominated by a few modes so that they can be easily excited. The modal theory for a scatterer is closely related to antenna resonance. An antenna is said to be resonant if its input reactance is zero, and the corresponding frequency at which the resonance occurs is called resonant frequency. Physically, this implies that stored electric field energy is equal to the stored magnetic field energy around the antenna.

There have been several modal theories for studying radiation problems (exterior boundary value problems). The temporal singularity expansion method (SEM) is based on the analysis in complex frequency domain [2]–[6]. The natural resonant frequencies arise from the requirement that a non-trivial current distribution exists on a conducting scatterer without incident fields, formulated by the electric field integral equation (EFIE) [7], [8]. The corresponding field patterns are called natural resonant modes. The natural resonant frequencies and natural resonant modes for dielectric bodies can be evaluated in terms of the Poggio, Miller, Chang, Harrington, Wu, and Tsai (PMCHWT) equations [9], [10]. The natural resonant modes are complex in SEM, which significantly increases the computational time and the difficulty in numerical implementations.

Another modal theory is called eigenmode expansion method (EEM), which expands the currents and the radiated fields in terms of the eigenmodes of an integral operator [11], [12]. The EEM may be considered as an extended theory of the temporal SEM. Same with the temporal SEM, the eigenvalues and the eigenmodes for EEM are complex numbers.

As another popular modal theory, the characteristic mode (CM) analysis is carried out in the real frequency domain [13]–[29], of which the characteristic values (eigenvalues) and characteristic modes are all real, and depend on

The associate editor coordinating the review of this manuscript and approving it for publication was Yuan Yao.

frequency. Generally, the characteristic values range from $-\infty$ to $+\infty$, among which those of smallest magnitudes are most important for radiation and scattering problems. The external resonant modes correspond to the zero characteristic values [29], and can be determined approximately by sweeping the frequency. It is noted that the CM formulations (as well as the temporal SEM and EEM formulations) depend on the medium properties of the scatterer. The characteristic modes for perfectly electric conducting (PEC) bodies are found by EFIE [13]–[16], while PMCHWT equations are applied to calculate the characteristic modes for dielectric and magnetic bodies [17]–[22]. The characteristic modes for the composite metallic-dielectric objects are obtained by the combinations of EFIE and PMCHWT equation [23]–[28]. To the best knowledge of the authors, there are no unified formulation that can simultaneously solve the CMs of scatterers with different medium parameters for now. The basic concepts of the temporal SEM, EEM, and CM techniques and their relationships have been discussed in [30].

All the aforementioned modal theories have their pros and cons. One common feature is that they are all related to the external resonant modes of the scatterer in a certain way. The external resonant modes, corresponding to the real resonant frequencies, are commonly used in antenna designs, and in many situations, antenna operates in the state of a single resonant mode. Multiple resonant modes are also frequently used for enhancing antenna bandwidth. For this reason, understanding the intrinsic resonances of scatterers is of vital importance in antenna design.

In this paper, we propose a unified procedure for evaluating the resonant modes for an arbitrary current source region, which is based on the expression for the difference between the stored electric and magnetic field energies. When the source region is assumed to be resonant, the condition that the difference between the stored electric and magnetic field energies vanishes leads to a homogeneous integral equation for the modal currents. After discretization, the integral equation is reduced to a real homogenous algebraic equation. By enforcing the condition that a non-trivial current distribution exits in the source region, the determinant of the coefficient matrix of the algebraic equation must be zero, which determines the resonant frequencies.

Compared with the modal theories studied previously, the theory of resonant modes (TRM) proposed in this paper determines the resonant modes based on the general expression for the difference of the stored field energies. Once the resonant modes are determined, the rest is to use excitations to realize the resonant modes in the selected source region. The paper is organized as follows. Section II presents the integral equation formulation and the implementation procedure for the determination of resonant modes in an arbitrary source region. Section III discusses the applications of the TRM in the design of antennas. A crossed-dipole antenna, a dual-band bowtie antenna, and a dual-band circular polarization (CP) antenna are designed in terms of the TRM and validated by simulations and experiments. Section IV compares the TRM with the temporal SEM, EEM, and CM from different aspects. Section V summarizes the main contributions of the paper.

II. THEORY OF RESONANT MODE

An antenna is said to be resonant if its input reactance is zero [31]. In this case, the stored electric field energy and the stored magnetic field energy around the antenna are equal. In general, an arbitrary scatterer (without an antenna input terminal) is said to be resonant if the stored electric field energy is equal to the stored magnetic field energy around the scatterer. It is this latter definition that we will use in this article.

A. FORMULATION

The concept of resonance can further be generalized to an arbitrary source region V_0 without reference to the medium properties in the source region. Figure 1 shows an arbitrary source region V_0 bounded by ∂V_0, in which a current distribution $\mathbf{J}$ is assumed to be confined in the source region in free space. It follows from the complex Poynting theorem that [32]

$$-\frac{1}{2}\int_{V_0}\bar{\mathbf{J}}\cdot\mathbf{E}dV(\mathbf{r})=\int_S\mathbf{u}_n\cdot\mathbf{S}dS+j2\omega\int_V(w_m-w_e)\,dV,\quad(1)$$

where $\mathbf{S}=\mathbf{E}\times\bar{\mathbf{H}}/2$ is the complex Poynting vector; $w_m=\mu_0\mathbf{H}\cdot\bar{\mathbf{H}}/4$ and $w_e=\varepsilon_0\mathbf{E}\cdot\bar{\mathbf{E}}/4$ are the magnetic and electric field energy densities; S is the boundary of a volume V containing the source region V_0, and a bar over a letter designates the complex conjugate operation. The left-hand side of (1) can be expressed as

$$-\frac{1}{2}\int_{V_0}\bar{\mathbf{J}}\cdot\mathbf{E}dV(\mathbf{r})=-\frac{1}{2}\int_{V_0}\bar{\mathbf{J}}\cdot(-\nabla\phi-j\omega\mathbf{A})dV(\mathbf{r}),\quad(2)$$

where ϕ and $\mathbf{A}$ are the scalar and vector potential functions

$$\phi(\mathbf{r})=\frac{\eta\nu}{4\pi}\int_{V_0}\frac{\rho(\mathbf{r}')e^{-jkR}}{R}dV(\mathbf{r}'),$$
$$\mathbf{A}(\mathbf{r})=\frac{\eta}{4\pi\nu}\int_{V_0}\frac{\mathbf{J}(\mathbf{r}')e^{-jkR}}{R}dV(\mathbf{r}'),$$

with $R=|\mathbf{r}-\mathbf{r}'|$, $\eta=\sqrt{\mu_0/\varepsilon_0}$ and $\nu=1/\sqrt{\mu_0\varepsilon_0}$. Inserting the above equations into (2) yields

$$\begin{aligned}-\frac{1}{2}&\int_{V_0}\bar{\mathbf{J}}\cdot\mathbf{E}dV(\mathbf{r})\\&=\frac{\omega\eta\nu}{8\pi}\int_{V_0}\int_{V_0}\left[\frac{1}{\nu^2}\frac{\bar{\mathbf{J}}(\mathbf{r})\cdot\mathbf{J}(\mathbf{r}')}{R}-\frac{\bar{\rho}(\mathbf{r})\rho(\mathbf{r}')}{R}\right]\\&\quad\times\sin(kR)dV(\mathbf{r})dV(\mathbf{r}')\\&\quad+j\frac{\omega\eta\nu}{8\pi}\int_{V_0}\int_{V_0}\left[\frac{1}{\nu^2}\frac{\bar{\mathbf{J}}(\mathbf{r})\cdot\mathbf{J}(\mathbf{r}')}{R}-\frac{\bar{\rho}(\mathbf{r})\rho(\mathbf{r}')}{R}\right]\\&\quad\times\cos(kR)dV(\mathbf{r})dV(\mathbf{r}').\end{aligned}$$

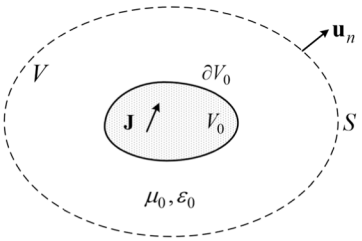

FIGURE 1. An arbitrary source region (without an input terminal) in free space.

From the above equation and (1), we obtain [1]

$$\tilde{W}_m - \tilde{W}_e = W_m - W_e = \frac{\eta}{16\pi\nu} \times \int_{V_0}\int_{V_0} \left[\bar{\mathbf{J}}(\mathbf{r}) \cdot \mathbf{J}(\mathbf{r}') + \frac{1}{k^2}\nabla \cdot \bar{\mathbf{J}}(\mathbf{r})\nabla' \cdot \mathbf{J}(\mathbf{r}')\right] \times \frac{\cos(kR)}{R} dV(\mathbf{r})dV(\mathbf{r}'), \quad (3)$$

where $\tilde{W}_m$ and $\tilde{W}_e$ stands for the total stored magnetic and electric field energies surrounding the source region (the radiator); and k is the wavenumber.

It is noted that the expression (3) can also be obtained by the general expressions for the stored energies around a radiator [33]. The difference between the stored field energies can be written as an inner product

$$\tilde{W}_m - \tilde{W}_e = (\hat{L}\mathbf{J}, \mathbf{J}), \quad (4)$$

where the integral operator $\hat{L}$ is defined by

$$\hat{L}\mathbf{J} = \frac{\eta}{16\pi\nu}\int_{V_0} [\mathbf{J}(\mathbf{r}') + \frac{1}{k^2}(\nabla' \cdot \mathbf{J}(\mathbf{r}'))\nabla]\frac{\cos(kR)}{R} dV(\mathbf{r}'). \quad (5)$$

The source region V_0 is said to be resonant if (4) vanishes. In order to find the resonant frequency and the corresponding current distribution $\mathbf{J}$ that makes (4) vanish, a sufficient condition is

$$\hat{L}\mathbf{J} = 0, \quad (6)$$

which is valid throughout the source region V_0. Apparently, the derivation of (6) does not rely on the medium parameters of the source region V_0. One can now follow the standard procedure of the method of moments (MoM) to solve (6) [34]. For simplicity, the source region V_0 will be assumed to be a surface in this paper, so that (6) becomes a surface integral equation. The current may be expanded in terms of the well-known Rao–Wilton–Glisson (RWG) basis functions $\mathbf{f_n}$ [35]

$$\mathbf{J} = \sum_{n=1}^{N} j_n \mathbf{f}_n. \quad (7)$$

Introducing (7) into (6), we obtain the following homogenous matrix equation by Galerkin method

$$[L(\omega)][J] = \mathbf{0}, \quad (8)$$

where $[J] = [j_1, j_2, \ldots, j_N]^T$, the matrix elements of $[L(\omega)]$ are given by

$$L_{mn} = \frac{\eta}{16\pi\nu}\int_{S_0}\int_{S_0}\left[\mathbf{f}_m(\mathbf{r}) \cdot \mathbf{f}_n(\mathbf{r}') - \frac{1}{k^2}\nabla' \cdot \mathbf{f}_n(\mathbf{r}')\nabla \cdot \mathbf{f}_m(\mathbf{r})\right] \times \frac{\cos(kR)}{R} dS(\mathbf{r})dS(\mathbf{r}'). \quad (9)$$

The necessary and sufficient condition for the existence of a non-zero solution of (8) is that the determinant of its coefficient matrix is zero

$$\det([L(\omega)]) = 0. \quad (10)$$

The above equation determines the resonant frequencies ω and the corresponding resonant current modes can be found from (8).

It is noted that (10) is a sufficient condition that makes (4) vanish. We now show that (10) is also a necessary condition. In fact, after following the above discretization, (4) can be written as a quadratic form

$$(\hat{L}\mathbf{J}, \mathbf{J}) = [J]^T[L][J]. \quad (11)$$

Since $[L]$ is symmetric, there exists an orthogonal matrix $[O]$ such that

$$[O]^T[L][O] = [D],$$

where $[D] = [\lambda_1, \lambda_2, \ldots, \lambda_N]^T$ is a diagonal matrix. Introducing a new vector $[Y] = [y_1, y_2, \ldots, y_n]^T$ defined by

$$[J] = [O][Y]$$

and substituting this into (11), we obtain

$$(\hat{L}\mathbf{J}, \mathbf{J}) = [Y]^T[D][Y] = \sum_{n=1}^{N} \lambda_n y_n^2. \quad (12)$$

If the above quadratic form is required to be zero for an arbitrary current distribution $\mathbf{J}$ (thus an arbitrary $[Y]$ by definition), we must have $\lambda_n = 0 (n = 1, 2, \ldots, N)$. This implies

$$\det[L] = \det[D] = \prod_{n=1}^{N} \lambda_n = 0 \quad (13)$$

since $[O]^T[O] = [I]$, where $[I]$ is the unit matrix of order N. Thus we have proved that (10) is also a necessary condition that make (4) vanish.

B. IMPLEMENTATION PROCEDURE

To evaluate the resonant modes for an arbitrary source region, the numerical solution process is implemented in *MATLAB* [36] and may be summarized into three steps.

1) *Discretization of the source region:* The open-source software *Gmsh* [37] is employed to generate the mesh of the source region.
2) *Determine the resonant frequencies:* The bisection method is applied to search the solutions of (10) in the selected frequency range.

TABLE 1. Convergence of the resonant frequencies between 1-5 GHz for rectangular plate.

Mesh Density	The Number of Triangular Elements	Resonant Frequencies (GHz)
$\lambda_{min}/8$	218	1.314/2.959/4.363/4.710/4.868
$\lambda_{min}/10$	320	1.315/2.965/4.527/4.782/4.853
$\lambda_{min}/15$	646	1.312/2.948/4.375/4.707/4.790
$\lambda_{min}/20$	**1248**	**1.313/2.945/ .374/ 4.706 /4.772**

3) *Visualize the resonant current modes and field patterns:* Resonant current modes can be obtained from (8) by using the *null* function in *MATLAB*, once the resonant frequencies ω are determined. The far-field pattern can be determined from the integral representation of the fields.

C. NUMERICAL EXAMPLE

In what follows, the source region V_0 will be called scatterer. To demonstrate the TRM, we will take a 100 mm $\times$ 40 mm rectangular plate as the scatterer to examine its resonant modes.

The resonant frequencies of the rectangular plate can be determined from (10). The first five resonant frequencies are listed in Table 1 in boldface, and the corresponding resonant modes (the modal current distributions) and their far-field patterns are shown in Figure 2. The first resonant mode is the fundamental mode, which is a half-wavelength mode along the long sides of the rectangular plate and vanishes at the two short ends. The second resonant mode is a full wavelength mode along the long sides and vanishes at the two short ends as well as in the middle of the plate. The third and the fourth resonant modes are resonated along the short sides of the rectangular plate. Note that the current directions along the two short sides for the third resonant mode are the same, while those for the fourth resonant mode are opposite. The fifth resonant mode is one-and-a-half-wavelength resonant mode along the long sides and the resonant current distribution has two zeros which divide the rectangular plate into three parts. The current direction of the central part is opposite to that of the other two parts.

Table 1 shows the convergence of the theory of the resonant modes as the mesh density increases. In general, using $\lambda_{min}/10$ (Here λ_{min} represents the wavelength corresponding to the highest frequency 5 GHz) as the mesh size is enough for the first resonant frequency. Finer meshes are needed for the higher order resonant frequencies.

D. DISCUSSION

The numerical implementation for the TRM is to find the zeros of a determinant which is similar to temporal SEM. However, the calculation of the external natural resonant mode for temporal SEM is carried out in complex frequency domain. Compared with TRM, the numerical solutions of the characteristic values and characteristic modes for CM are first obtained from a generalized eigenvalue equation, and then

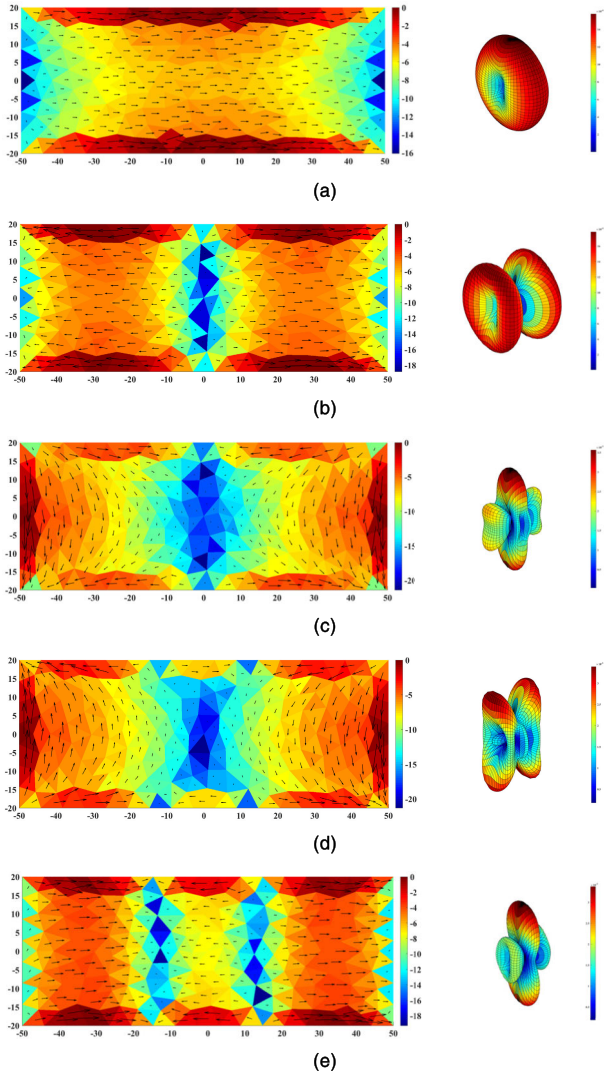

FIGURE 2. Modal currents distributions and their far-field patterns for the rectangular plate.

one needs to sort and track the characteristic values in a wide frequency band. Only the frequencies with the characteristic values close to zero can be considered as the resonant frequencies. In addition, many non-resonance modes (inductive modes and capacitive modes) are obtained by the temporal SEM and CM, which not only increase the computational time and difficulty, but also cause many confusions for the antenna designers while these modes are applied to enhance the antenna bandwidth.

The TRM directly determines the resonant modes from the difference of the stored field energies. Once the resonant modes are determined, the rest is to use various excitations to realize the resonant current modes in the selected source region.

III. APPLICATIONS OF THE RESONANT MODES

In many applications, antenna operates in the state of a single resonant mode, while multiple resonant modes are often used

to enhance antenna bandwidth. In this paper, we focus on the realization of modal currents by planar metal conductors via proper excitations for easy implementation. In what follows, we will demonstrate the applications of the TRM in the design of antennas through three examples: a crossed-dipole antenna, a dual-band bowtie antenna, and a dual-band circular polarization antenna. The resonant current modes are first determined by TRM. Input terminals are then introduced and positioned at the maximum of the current modes to excite the corresponding field modes. To validate TRM, the three examples are also simulated by the Integral Equation Solver Module in CST Studio [38] and further verified by experiments.

A. CROSSED-DIPOLE ANTENNA

The idea of crossed-dipole antenna was originated from a circular polarization (CP) antenna, proposed by Bolster in 1961 [39]. Although the crossed-dipole antenna was theorized in [39] and demonstrated experimentally in [40], there was barely a theory that explains clearly about its resonant properties.

Consider a cross (i.e., the source region V_0) consisting of two planar metal strips shown in Figure 3(a), where the lengths of the horizontal and vertical strips are $l_1 = 118$ mm and $l_2 = 97$ mm respectively, and the width of the strips is set as $w = 2$ mm.

1) RESONANT MODES

From (10), the first three resonant frequencies of the cross are found to be 1.190 GHz, 1.428 GHz, and 1.443 GHz, respectively. The corresponding modal current distributions are depicted in Figure 3 (b) to Figure 3(d). As shown in Figure 3(b), the fundamental (the first) modal current concentrates on the horizontal strip. In contrast, the third modal current is along the vertical dipole, as indicated by Figure 3(d). The second modal current, shown in Figure 3(c), has a distribution that is quite different from the first and the third. It has two different current paths. The first path consists of the top vertical arm and the right horizontal arm of the cross and the second path consists of the bottom vertical arm and left horizontal arm.

2) SIMULATION AND MEASURED RESULTS

We now use the first and the third mode of the cross to build a CP antenna. As indicated in Figure 3, the maximum values of first and third modal current are right at the center of the cross. To excite these two modes, a voltage source is introduced at the center of the cross. For this purpose, the cross is broken into two separate parts to form a crossed-dipole antenna. The first part consists of the top vertical arm and the right horizontal arm, and the second part consists of the bottom vertical arm and the left horizontal arm, with a small gap at the center of the cross (see the inset of Figure 6(a)). A discrete face port with 50 Ohm is applied across the gap in the simulation with CST Studio to excite the first and third modes simultaneously.

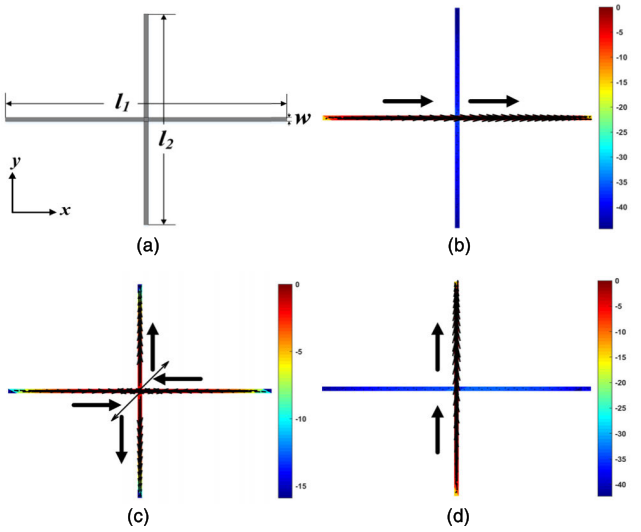

FIGURE 3. A cross and its modal currents. (a) Dimensions. (b) Modal current at 1.190 GHz. (c) Modal current at 1.427 GHz. (d) Modal current at 1.440 GHz.

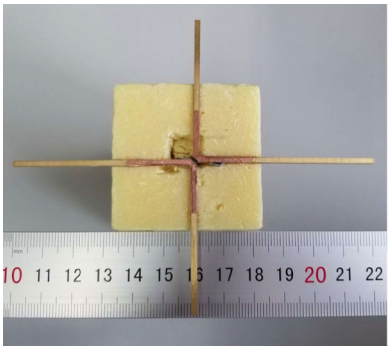

FIGURE 4. Photograph of the fabricated CP crossed-dipole antenna.

The fabricated crossed-dipole antenna is shown in Figure 4. Figure 5 is the reflection coefficient and axis ratio value of the crossed-dipole antenna. Two distinct reflection zeros occur approximately around the first and third resonant frequencies in the simulated and measured results. The measured reflection coefficient and axis ratio all agree with the simulated results. The fractional bandwidth (FBW) of the crossed-dipole antenna is 26.6% at -10dB of the reflection coefficient. The bandwidth of the 3dB axis ratio in the direction of ($\theta = 0°, \varphi = 0°$) is 6.1%, which is comparable with the same type of CP antennas [41], [42]. The antenna exhibits a bidirectional radiation pattern. In the direction of $\theta = 0°$, it generates a left-hand circularly polarized (LHCP) wave, while in the direction of $\theta = 180°$, the radiated wave exhibits a right-handed circularly polarized (RHCP) behavior. More CP characteristics about the crossed dipole antenna can be found in [40].

Figure 6 shows the simulated resonant current distributions of the crossed dipole at the two reflection zeros shown in Figure 5(a). As expected, the resonant current at the first reflection zero mainly concentrates on the two horizontal

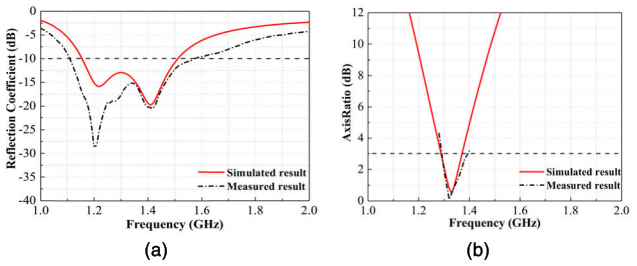

FIGURE 5. Simulated and measured results of CP crossed-dipole antenna. (a) Reflection coefficient. (b) Axis ratio in the direction ($\theta = 0°, \varphi = 0°$).

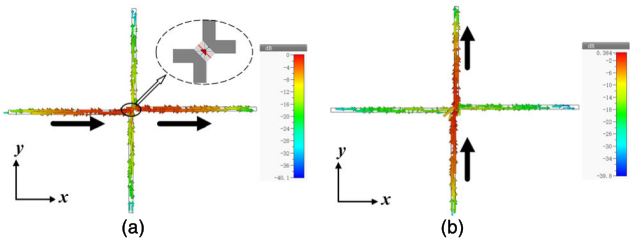

FIGURE 6. Simulated resonant currents at (a) 1.22 GHz. (b) 1.42 GHz.

arms (see Figure 6(a)) while the resonant current at the second reflection zero is mainly distributed on the vertical dipole (Figure 6(b)), agreeing with the simulated modal current distributions shown in Figure 3.

The radiation patterns at *xoz*-plane and *yoz*-plane for the first and third modal currents from the proposed modal theory are compared with the CST simulations and the measured ones in Figure 7. Figure 7(a) and Figure 7(b) indicate that the radiation patterns from the proposed modal theory, the CST simulation, and measured ones agree well at the first resonant frequency. The maximum gains from the proposed modal theory, the CST simulation, and the measured ones at the two cut planes are respectively 2.10 dB, 2.14 dB, and 2.17 dB. The radiation patterns in Figure 7(a) and Figure 7(b) also indicates that the radiation at the first resonant frequency mainly comes from the two horizontal arms. Similar results can be found in Figure 7(c) and Figure 7(d). In this case, radiation mainly comes from the two vertical arms.

For the crossed-dipole antenna, the two vertical or horizontal arms do not exactly form a straight line as in Figure 7(a) due to the introduction of a feeding gap. As shown in Figure 7(a) and Figure 7(d), the difference of the patterns appearing in x-direction or y-direction between proposed modal theory, the CST simulation, and the measured results is most likely caused by the small alteration of the geometry from the original cross to the crossed-dipole antenna (with the feeding gap), which brings a perpendicular feeding component for the vertical strip (horizontal strip) at the first (second) resonant frequency. The perpendicular feeding components also lead to the unexpected currents that either distributes along the vertical strip in Figure 6(a) or the horizontal strip in Figure 6(b).

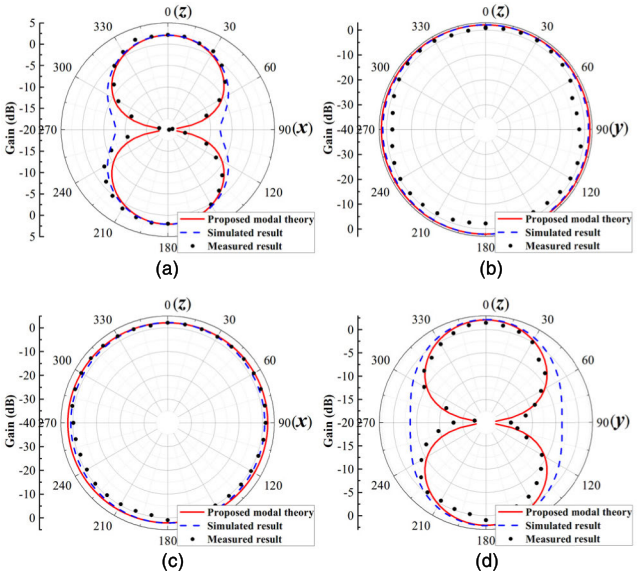

FIGURE 7. Comparisons of radiation patterns between proposed modal theory, the CST simulation, and measured results. (a) Patterns at xoz-plane at first resonant frequency. (b) Patterns at yoz-plane at first resonant frequency. (c) Patterns at xoz-plane at third resonant frequency. (d) Patterns at yoz-plane at third resonant frequency.

TABLE 2. Parameters of dual-band bowtie antenna.

Parameter	Value (mm)
w	30
l	90
t	4
l_s	20
w_s	3
t_s	3
g_s	12

B. DUAL-BAND BOWTIE ANTENNA

A bowtie antenna is often used for wideband applications, and its wideband characteristic is determined by the flare angle and the size of the structure [43], [44]. We now apply the theory of resonant modes to the design of a dual-band bowtie antenna with a fixed flare angle and size. Consider a planar slotted bowtie (without a feeding mechanism) shown in Figure 8(a), whose geometrical parameters are listed in Table 2.

1) RESONANT MODES

From (10), the first three resonant frequencies are found to be 1.123 GHz, 2.521 GHz, and 3.568 GHz, and the corresponding modal currents are plotted in Figure 8(b)-(d). The first modal current distribution at 1.123 GHz is along the two long edges of slotted bowtie, which is similar to a half-wavelength dipole. The second modal current distribution is similar to a full-wavelength dipole while the third modal current distribution to a one-and-half-wavelength dipole.

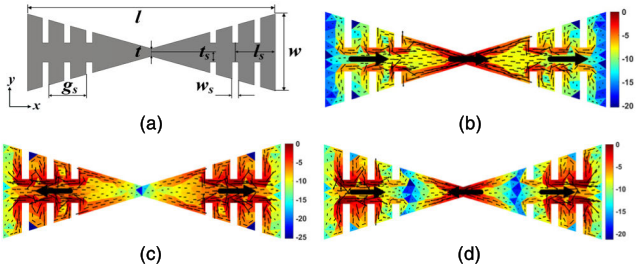

FIGURE 8. Planar slotted bowtie and the modal current distributions. (a) Dimensions. (b) Modal current at 1.123 GHz. (c) Modal current at 2.521 GHz. (d) Modal current at 3.568 GHz.

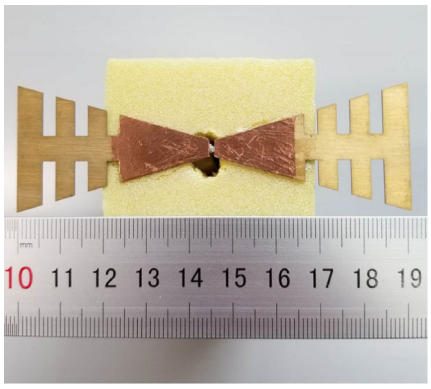

FIGURE 9. Photograph of the fabricated dual-band bowtie antenna.

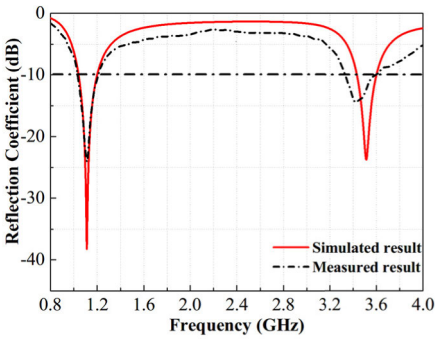

FIGURE 10. Simulated and measured reflection coefficients of dual-band bowtie antenna.

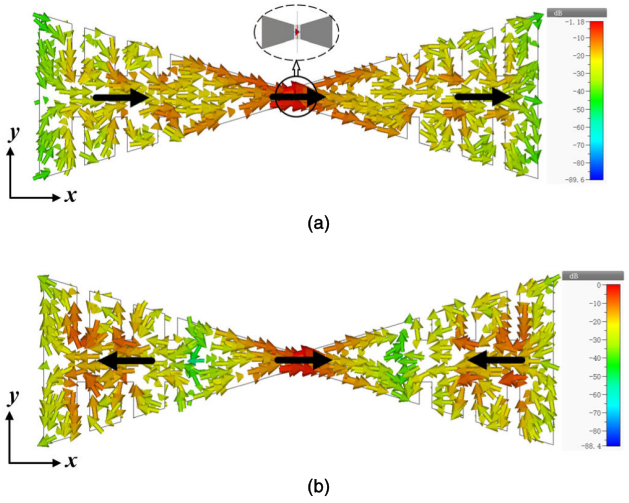

FIGURE 11. Simulated resonant currents at (a) 1.111 GHz. (b) 3.514 GHz.

2) SIMULATION AND MEASURED RESULTS

We now break the slotted bowtie structure into two separate parts and introduce a small gap in the middle of the bowtie. To excite the first and third modes of the slotted bowtie, a discrete face port with 50 Ohm is applied across the gap to form a dual-band bowtie antenna.

The fabricated dual-band bowtie antenna is presented in Figure 9. The simulated and measured reflection coefficients of the dual-band slotted bowtie antenna are shown in Figure 10, in which two reflection zeros occur at 1.111 and 3.514 GHz in simulation, very close to the first and third modal resonant frequencies. The measured reflection coefficient indicates that the first resonant frequency is identical with simulated one while there is a small deviation between the measured and the simulated results for the second resonant frequency, which may be caused by fabrication error of the antenna and the feeding gap introduced in order to build an antenna. The simulated resonant current distributions at the center frequencies of the two bands are shown in Figure 11, agreeing well with the modal currents demonstrated in in Figure 8.

The radiation patterns for the modal currents at the first and third resonant frequencies are compared with the CST simulations and the measurements, and are shown in Figure 12. The simulated and measured radiation patterns at xoz-plane and yoz-plane at the first resonant frequency are depicted in Figure 12(a) and Figure 12(b) and agree well with those obtained from the theory of resonant modes. Similar results can be found in Figure 12(c) and Figure 12(d) for the third resonant frequency. The slight difference of the radiation patterns between the proposed modal theory and the simulated results with CST at the third resonant frequency is most likely caused by the small feeding gap introduced to feed the slotted bowtie.

C. DUAL-BAND CP ANTENNA

We now combine the slotted bowtie element with the crossed-dipole element to form a dual-band CP antenna. As shown in Figure 13(a), the slotted bowtie element is set in the horizontal direction and the crossed-dipole element is placed in the vertical direction. The detailed dimensions of this new cross structure are listed in Table 3.

1) RESONANT MODES

The first seven resonant frequencies of the new cross structure are found to be 1.022 GHz, 1.212 GHZ, 1.261 GHz, 2.841 GHz, 3.498 GHZ, 3.763 GHz, and 3.922 GHz, respectively. The corresponding modal current distributions are shown in Figure 13(b) to Figure 13(h). The modal current in Figure 13(b) is mainly distributed on the surface of the

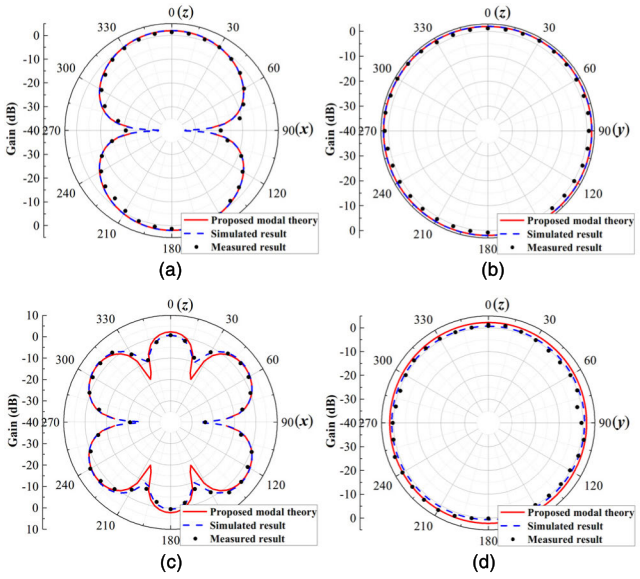

FIGURE 12. Comparisons of radiation patterns from proposed modal theory, the CST simulation, and the measured results. (a) Patterns at xoz-plane at first resonant frequency. (b) Patterns at yoz-plane at first resonant frequency. (c) Patterns at xoz-plane at third resonant frequency. (d) Patterns at yoz-plane at third resonant frequency.

TABLE 3. Parameters of dual-band dual-mode dual circular polarization antenna.

Parameter	Value (mm)
l_b	96
w_b	32
l_d	116
w_d	2
w_{s_b}	3
l_{s_b}	16
t_{s_b}	4
g_{s_b}	15
g	3

bowtie element, exhibiting a half-wavelength resonant mode. A similar distribution is also shown in Figure 13(f), which is the one-and-a-half wavelength resonant mode of the bowtie element. In contrast, the modal current distributions in Figure 13(c) and Figure 13(g) mostly concentrate on the vertical dipole element, and the current distributions on the bowtie element are very weak. Figure 13(c) is a half-wavelength resonant mode of the vertical dipole element and Figure 13(g) is a one-and-a-half wavelength resonant mode of the vertical dipole element. In addition, one common feature found in Figure 13(b), Figure 13(c), Figure 13(f), and Figure 13(g) is that the maximum currents occur at the intersection of the horizontal bowtie element and the vertical dipole element. The fourth modal current distribution in Figure 13(e) has a minimum current value at the intersection instead, while the modal current distributions in Figure 13(d) and Figure 13(h) change directions at the intersection.

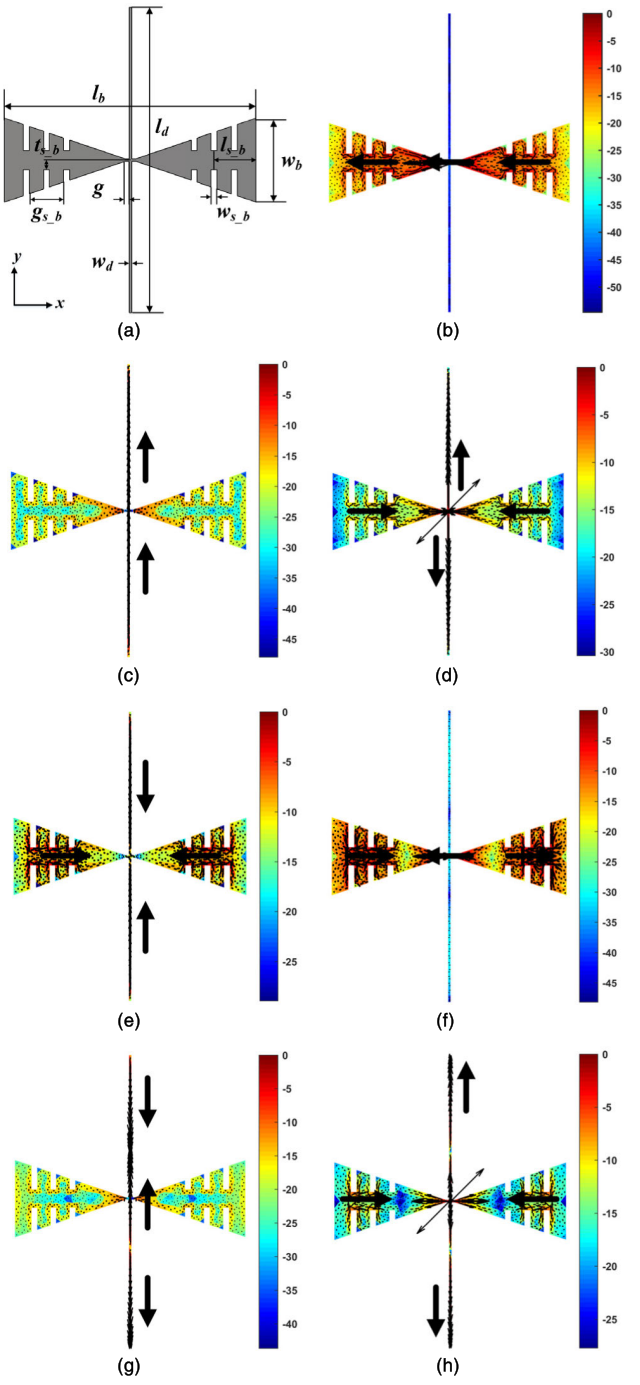

FIGURE 13. The cross scatter and its modal currents. (a) Dimensions. (b) Modal current at 1.022 GHz. (c) Modal current at 1.212 GHz. (d) Modal current at 1.261 GHz. (e) Modal current at 2.841 GHz. (f) Modal current at 3.498 GHz. (g) Modal current at 3.763 GHz. (h) Modal current at 3.922 GHz.

2) SIMULATION AND MEASURED RESULTS

To realize a dual-band CP antenna, we separate the structure in Figure 13(a) into two parts. The first part consists of the top vertical dipole arm and the left horizontal bowtie arm, and the second part consists of the bottom vertical dipole arm and the right horizontal bowtie arm, with a small gap at the center of the structure (see the inset of Figure 16).

A discrete face port with 50 Ohm is applied across the gap in the CST simulation to excite the first resonant mode, second resonant mode, fifth resonant mode and sixth resonant mode simultaneously.

Figure 14 is the photograph of the fabricated dual-band CP antenna. The simulated and measured reflection coefficients and the axis ratio of the antenna are shown in Figure 15. It can be seen that each band has two reflection zeros. The simulation indicates that four reflection zeros occur at 1.08 GHz, 1.14 GHz, 3.46 GHz, and 3.68 GHz, very close to the first resonant mode, second resonant mode, fifth resonant mode and sixth resonant mode. The antenna covers the frequency bands from 0.983 GHz to 1.265 GHz and 3.362 GHz to 3.763 GHz. The fractional bandwidths of the two bands are 25.09% and 11.26% respectively. The simulated 3-dB axis ratio bandwidths in the direction of ($\theta = 0°$, $\varphi = 0°$) are from 1.111 GHz to 1.164 GHz (4.66%) and 3.530 GHz to 3.604 GHz (2.07%) with two CP center frequencies at 1.14 GHz and 3.57 GHz, respectively. The dual-band CP antenna also exhibits a bidirectional radiation pattern, similar to the crossed-dipole antenna. However, the dual-band CP antenna exhibits a RHCP behavior in the direction of $\theta = 0°$ and a LHCP characteristic in the direction of $\theta = 180°$, due to the position change of the longer dipole element.

The resonant current distributions at the four reflection zeros are presented in Figure 16. The half-wavelength resonant mode and the one-and-a-half-wavelength resonant mode of the horizontal bowtie element are shown in Figure 16(a) and Figure 16(c). The similar modal current distributions for the vertical dipole element can be found in Figure 16(b) and Figure 16(d). Comparing with the resonant modal current distributions in Figure 13(b) and Figure 13(f), unexpected current components appear on the vertical dipole elements as shown in Figure 16(a) and Figure 16(c). These unexpected current components are attributed to the feeding gap introduced to build the antenna. The discrete port (see the inset of Figure 16) brings a vertical current component for the vertical dipole element during the excitation processes of resonant modes of the horizontal bowtie element in Figure 16(a) and Figure 16(c). Similar phenomena are seen in Figure 16(b) and Figure 16(d) when the resonant modes of the vertical dipole are excited.

Figure 17 shows the radiation patterns at *xoz*-plane and *yoz*-plane for the first mode, second mode, fifth mode and sixth mode obtained from the proposed modal theory, the CST simulation, and the measurements. It can be seen that the simulated and measured radiation patterns agree well with those from the proposed modal theory. The slight differences are due to the unexpected current distributions caused by the feeding gap as mentioned above.

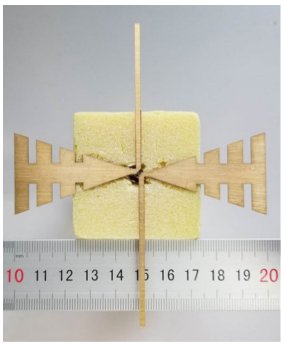

FIGURE 14. Photograph of the fabricated dual-band CP antenna.

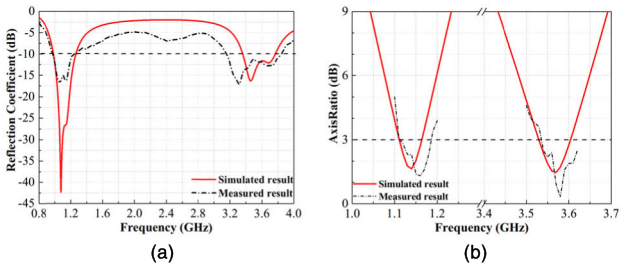

FIGURE 15. Simulated and measured results of the dual band CP antenna. (a) Reflection coefficient. (b) Axis ratio value in the direction ($\theta = 0°$, $\varphi = 0°$).

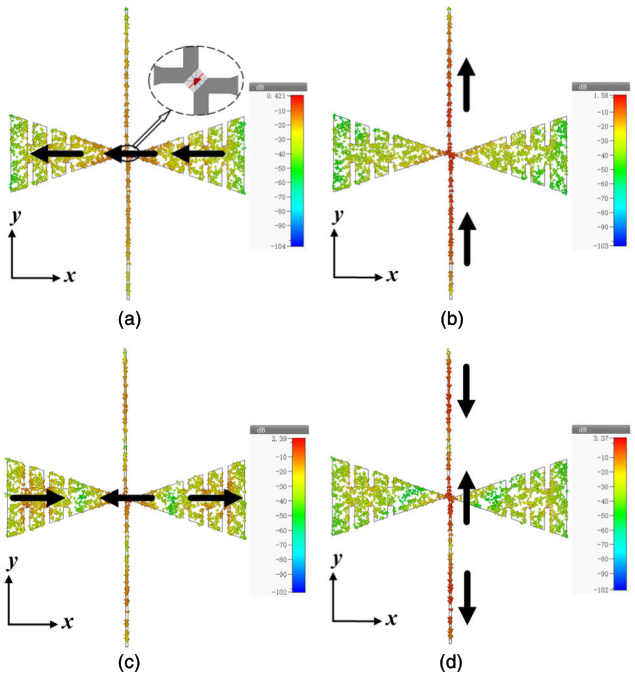

FIGURE 16. Simulated resonant currents at (a) 1.08 GHz. (b) 1.14 GHz. (c) 3.46 GHz. (d) 3.68 GHz.

IV. COMPARISONS AND DISCUSSIONS

The temporal SEM, EEM, CM and TRM all belong to the external resonant modes and are useful in providing guidelines for antenna design. However, the external resonant modes for TRM are quite different from the resonant modes resulted from three other methods for its mathematical formulation and physical implication. The logic behind TRM is to find the possible (intrinsic) current distributions in a selected geometry. The current distributions are then realized

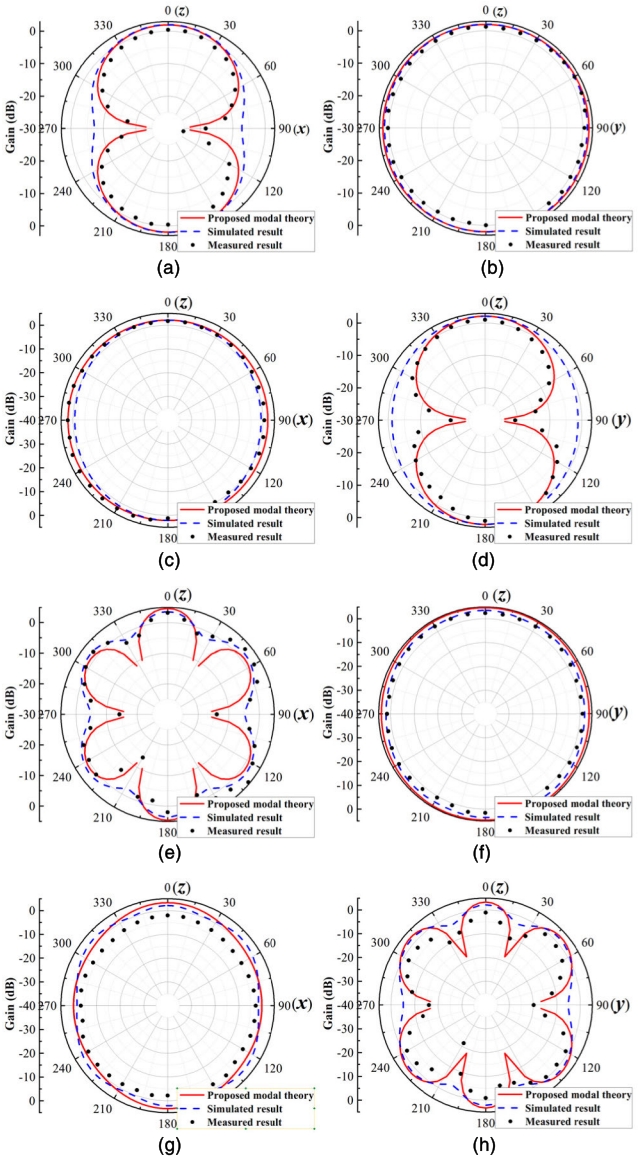

FIGURE 17. Comparisons of radiation patterns from proposed modal theory, the CST simulation, and the measured results. (a) Patterns at xoz-plane at first resonant frequency. (b) Patterns at yoz-plane at first resonant frequency. (c) Patterns at xoz-plane at second resonant frequency. (d) Patterns at yoz-plane at second resonant frequency. (e) Patterns at xoz-plane at fifth resonant frequency. (f) Patterns at yoz-plane at fifth resonant frequency. (g) Patterns at xoz-plane at sixth resonant frequency. (h) Patterns at yoz-plane at sixth resonant frequency.

by antenna designs through introducing input port (exciting source) in a material body (such as a metal) that occupies the selected geometry. There have been different ways to realize a current distribution. For example, one can also use an antenna array to approximate a continuous current distribution. Some comparisons between TRM and three other modal theories are presented in Table 4.

The external resonant modes for temporal SEM ($\mathbf{J}^{\mathbf{SEM}}$) are determined by seeking the zeros of the determinant of various impedance Z operator defined by the boundary condition (BC) in various mediums [7]–[10]. The external resonant

TABLE 4. Comparisons of different modal theories for external resonant modes.

Theory	Equation	Numerical Solution	Physical Basis
Temporal SEM	$Z\mathbf{J}^{\mathbf{SEM}} = \mathbf{0}$	$\det(Z) = 0$	BC
EEM	$Z\mathbf{J}_n^{\mathbf{EEM}} = v_n \mathbf{J}_n^{\mathbf{EEM}}$	$v_n = 0$	BC
CM	$X\mathbf{J}_n^{\mathbf{CM}} = \lambda_n R\mathbf{J}_n^{\mathbf{CM}}$	$\lambda_n = 0$	BC
TRM	$\hat{L}\mathbf{J}^{\mathbf{TRM}} = \mathbf{0}$	$\det(\hat{L}) = 0$	**DSFE***

DSFE*: **D**ifference of **S**tored **F**ield **E**nergies

modes for EEM ($\mathbf{J}_n^{\mathbf{EEM}}$) [11], [12] are evaluated equivalently by seeking the zeros of the eigenvalues ($v_n = 0$). The modal theories of the temporal SEM and EEM are all confined in complex frequency domain, which may significantly increase computational time and implementation difficulty.

CM [15]–[28] makes use of the real part R and the imaginary part X of the impedance operator Z ($Z = R + jX$) to solve a generalized eigenvalue equation that determines the real characteristic values λ_n and the real characteristic modes $\mathbf{J}_n^{\mathbf{CM}}$ for a given frequency. One needs to sort and track the characteristic values in a wide frequency band and only the frequencies with the lowest characteristic values (close to zero) can be considered as the resonant frequencies. The complex operators of Z for CM are also developed from the boundary conditions, which depend on the medium properties of the source region.

Distinguished from the other three modal theories, the mathematical formulation for the TRM is based on the general expression for the difference between the stored electric and magnetic field energies in terms of the source current distribution instead of the boundary conditions used in other modal theories. Once the modal currents are determined, the rest is to use various techniques to realize the current distributions.

V. CONCLUSION

In this paper, a new modal theory is proposed in terms of the general expression of the difference between the stored magnetic and electric field energies. Different from those modal theories that expand the fields by a linear combination of fundamental field patterns (modes) constrained by the boundary conditions, the new modal theory directly determines the resonant modes for an arbitrary source region without using the concept of inductive or capacitive modes. The resonant frequencies and the corresponding resonant modes are determined by requiring that a non-trivial solution exists for a homogeneous integral equation, which can be discretized into a real homogenous algebraic equation by a standard MoM procedure. To validate the proposed modal theory, a crossed-dipole antenna, a dual-band bowtie antenna and a dual band

CP antenna have been designed by the new modal theory to achieve various functions.

ACKNOWLEDGMENT

The authors would like to thank Prof. D. G. Fang of Nanjing University of Science and Technology for his valuable comments.

REFERENCES

[1] W. Geyi, *Foundations of Applied Electrodynamics*. Hoboken, NJ, USA: Wiley, 2010, Ch. 4.
[2] C. E. Baum, "On the singularity expansion method for the solution of electromagnetic interaction problems," AFWL, Interact. Notes 88, Dec. 1971.
[3] C. E. Baum, "The singularity expansion method," in *Transient Electromagnetic Fields*. New York, NY, USA: Springer-Verlag, 1976, pp. 129–179.
[4] A. Ramm, "Theoretical and practical aspects of singularity and eigenmode expansion methods," *IEEE Trans. Antennas Propag.*, vol. AP-28, no. 6, pp. 897–901, Nov. 1980.
[5] A. G. Ramm, "Mathematical foundations of the singularity and eigenmode expansion methods (SEM and EEM)," *J. Math. Anal. Appl.*, vol. 86, no. 2, pp. 562–591, Apr. 1982.
[6] L. Marin, "Natural-mode representation of transient scattered fields," *IEEE Trans. Antennas Propag.*, vol. AP-21, no. 6, pp. 809–818, Nov. 1973.
[7] W. Sun, K. M. Chen, D. P. Nyquist, and E. J. Rothwell, "Determination of the natural modes for a rectangular plate (transient scattering)," *IEEE Trans. Antennas Propag.*, vol. 38, no. 5, pp. 643–652, May 1990.
[8] Y. Long, "Determination of the natural frequencies for conducting rectangular boxes," *IEEE Trans. Antennas Propag.*, vol. 42, no. 7, pp. 1016–1021, Jul. 1994.
[9] A. W. Glisson, D. Kajfez, and J. James, "Evaluation of modes in dielectric resonators using a surface integral equation formulation," *IEEE Trans. Microw. Theory Techn.*, vol. 31, no. 12, pp. 1023–1029, Dec. 1983.
[10] D. Kajfez, A. W. Glisson, and J. James, "Computed modal field distributions for isolated dielectric resonators," *IEEE Trans. Microw. Theory Techn.*, vol. 32, no. 12, pp. 1609–1616, Dec. 1984.
[11] C. E. Baum, "On the eigenmode expansion method for electromagnetic scattering and antenna problems, Part I: Some basic relations for eigenmode expansions and their relation to the singularity expansion," Air Force Weapons Lab., Kirtland Air Force Base, Albuquerque, NM, USA, Interact. Note 229, Jan. 1975.
[12] C. E. Baum, "Emerging technology for transient and broad-band analysis and synthesis of antennas and scatterers," *Proc. IEEE*, vol. 64, no. 11, pp. 1598–1616, Nov. 1976.
[13] R. J. Garbacz, "Modal expansions for resonance scattering phenomena," *Proc. IEEE*, vol. 53, no. 8, pp. 856–864, Aug. 1965.
[14] R. J. Garbacz and R. Turpin, "A generalized expansion for radiated and scattered fields," *IEEE Trans. Antennas Propag.*, vol. 19, no. 3, pp. 348–358, May 1971.
[15] R. F. Harrington and J. R. Mautz, "Theory of characteristic modes for conducting bodies," *IEEE Trans. Antennas Propag.*, vol. 19, no. 5, pp. 622–628, Sep. 1971.
[16] R. F. Harrington and J. R. Mautz, "Computation of characteristic modes for conducting bodies," *IEEE Trans. Antennas Propag.*, vol. 19, no. 5, pp. 629–639, Sep. 1971.
[17] R. F. Harrington, J. R. Mautz, and Y. Chang, "Characteristic modes for dielectric and magnetic bodies," *IEEE Trans. Antennas Propag.*, vol. 20, no. 2, pp. 194–198, Mar. 1972.
[18] Y. Chang and R. F. Harrington, "A surface formulation for characteristic modes of material bodies," *IEEE Trans. Antennas Propag.*, vol. 25, no. 6, pp. 789–795, Nov. 1977.
[19] Y. Chen, "Alternative surface integral equation-based characteristic mode analysis of dielectric resonator antennas," *IET Microw., Antennas Propag.*, vol. 10, no. 2, pp. 193–201, Jan. 2016.
[20] F.-G. Hu and C.-F. Wang, "FE-BI formulations for characteristic modes," *IEEE Trans. Microw. Theory Techn.*, vol. 64, no. 5, pp. 1396–1401, May 2016.
[21] R. Lian, J. Pan, and S. Huang, "Alternative surface integral equation formulations for characteristic modes of dielectric and magnetic bodies," *IEEE Trans. Antennas Propag.*, vol. 65, no. 9, pp. 4706–4716, Sep. 2017.
[22] Z. T. Miers and B. K. Lau, "Computational analysis and verifications of characteristic modes in real materials," *IEEE Trans. Antennas Propag.*, vol. 64, no. 7, pp. 2595–2607, Jul. 2016.
[23] P. Ylä-Oijala, "Generalized theory of characteristic modes," *IEEE Trans. Antennas Propag.*, vol. 67, no. 6, pp. 3915–3923, Jun. 2019.
[24] L. Guo, Y. Chen, and S. Yang, "Characteristic mode formulation for dielectric coated conducting bodies," *IEEE Trans. Antennas Propag.*, vol. 65, no. 3, pp. 1248–1258, Mar. 2017.
[25] L. Guo, Y. Chen, and S. Yang, "Generalized characteristic-mode formulation for composite structures with arbitrarily metallic–dielectric combinations," *IEEE Trans. Antennas Propag.*, vol. 66, no. 7, pp. 3556–3566, Jul. 2018.
[26] S. Huang, J. Pan, Y. Luo, and D. Yang, "Single-source surface integral equation formulations for characteristic modes of fully dielectric-coated objects," *IEEE Trans. Antennas Propag.*, vol. 67, no. 7, pp. 4914–4919, Jul. 2019.
[27] Q. Wu, "General metallic-dielectric structures: A characteristic mode analysis using volume-surface formulations," *IEEE Antennas Propag. Mag.*, vol. 61, no. 3, pp. 27–36, Jun. 2019.
[28] P. Yla-Oijala, A. Lehtovuori, H. Wallen, and V. Viikari, "Coupling of characteristic modes on PEC and lossy dielectric structures," *IEEE Trans. Antennas Propag.*, vol. 67, no. 4, pp. 2565–2573, Apr. 2019.
[29] Y. Chen, and C.-F. Wang, *Characteristic Modes: Theory and Applications in Antenna Engineering*. Hoboken, NJ, USA: Wiley, 2015.
[30] S. Huang, J. Pan, and Y. Luo, "Study on the relationships between eigenmodes, natural modes, and characteristic modes of perfectly electric conducting bodies," *Int. J. Antennas Propag.*, vol. 2018, pp. 1–13, 2018, 8735635.
[31] W. L. Stutzman and G. A. Thiele, *Antenna Theory and Design*. 2nd ed. New York, NY, USA: Wiley, 1998, Ch. 5.
[32] R. F. Harrington, *Time-Harmonic Electromagnetic Fields*. Hoboken, NJ, USA: Wiley, 2001.
[33] W. Geyi, "Stored energies and radiation Q," *IEEE Trans. Antennas Propag.*, vol. 63, no. 2, pp. 636–645, Feb. 2015.
[34] R. F. Harrington, *Field Computation by Moment Methods*. Hoboken, NJ, USA: Wiley, 1993.
[35] S. M. Rao, D. R. Wilton, and A. W. Glisson, "Electromagnetic scattering by surfaces of arbitrary shape," *IEEE Trans. Antennas Propag.*, vol. 30, no. 3, pp. 409–418, May 1982.
[36] MathWorks. (2018). *The MATLAB*. [Online]. Available: https://www.mathworks.com
[37] C. Geuzaine and J.-F. Remacle, "Gmsh: A 3-D finite element mesh generator with built-in pre- and post-processing facilities," *Int. J. Numer. Methods Eng.*, vol. 79, no. 11, pp. 1309–1331, 2009.
[38] (Oct. 2018). *CST Computer Simulation Technology AG*. USA. [Online]. Available: https://www.cst.com
[39] M. F. Bolster, "A new type of circular polarizer using crossed dipoles," *IRE Trans. Microw. Theory Techn.*, vol. 9, no. 5, pp. 385–388, Sep. 1961.
[40] B. Y. Toh, R. Cahill, and V. F. Fusco, "Understanding and measuring circular polarization," *IEEE Trans. Educ.*, vol. 46, no. 3, pp. 313–318, Aug. 2003.
[41] S. X. Ta, J. J. Han, and I. Park, "Compact circularly polarized composite cavity-backed crossed dipole for GPS applications," *J. Electromag. Eng. Sci.*, vol. 13, no. 1, pp. 44–49, Mar. 2013.
[42] S. X. Ta and I. Park, "Dual-band low-profile crossed asymmetric dipole antenna on dual-band AMC surface," *IEEE Antennas Wireless Propag. Lett.*, vol. 13, pp. 587–590, Apr. 2014.
[43] C. J. Leat, N. V. Shuley, and G. F. Stickley, "Triangular-patch model of bowtie antennas: Validation against Brown and Woodward," *IEE Proc. Microw., Antennas Propag.*, vol. 145, no. 6, pp. 465–470, Dec. 1998.
[44] S. N. Makarov, *Antenna and EM Modeling With MATLAB*. Hoboken, NJ, USA: Wiley, 2002.

RUQI XIAO was born in Jiangsu, China, in 1993. He received the B.E. degree in electronic science and technology from Binjiang College, Nanjing University of Information Science and Technology (NUIST), Nanjing, China, in 2015, where he is currently pursuing the Ph.D. degree.

His current research interests include resonant antennas, filtering antennas, and passive RF components.

WEN GEYI (Fellow, IEEE) was born in Ping Jiang, China, in 1963. He received the B.Eng., M.Eng., and Ph.D. degrees in electrical engineering from Xidian University, Xi'an, China, in 1982, 1984, and 1987, respectively. From 1988 to 1990, he was a Lecturer with the Radio Engineering Department, Southeast University, Nanjing, China. From 1990 to 1992, he was an Associate Professor with the Institute of Applied Physics, University of Electronic Science and Technology of China (UESTC), Chengdu, China. From 1992 to 1993, he was a Visiting Researcher with the Department of Electrical and Computer Engineering, University of California at Berkeley, Berkeley, CA, USA. He was a Full Professor, from 1993 to 1998; the Vice Chairman, from 1996 to 1997; and the Chairman, from 1997 to 1998, with the Institute of Applied Physics, UESTC. He was a Visiting Professor with the Electrical Engineering Department, University of Waterloo, Waterloo, ON, Canada, from February 1998 to May 1998. From 1998 to 2007, he was with Blackberry, Ltd., Waterloo, first as a Senior Scientist with the Radio Frequency Department, and then as the Director of the Advanced Technology Department. Since 2010, he has been a National Distinguished Professor with Fudan University, Shanghai, China, and the Nanjing University of Information Science and Technology (NUIST), Nanjing, where he is currently the Director of the Research Center of Applied Electromagnetics. He has authored over 100 journal publications and *Foundations for Radio Frequency Engineering* (World Scientific, 2015), *Foundations of Applied Electrodynamics* (Wiley, 2010), *Advanced Electromagnetic Field Theory* (National Defense Publishing House, China, 1999), and *Modern Methods for Electromagnetic Computations* (Henan Science and Technology Press, China, 1994). He holds more than 40 patents. His current research interests include microwave theory and techniques, and antennas and wave propagation.

WEN WU (Senior Member, IEEE) received the Ph.D. degree in electromagnetic field and microwave technology from Southeast University, Nanjing, China, in 1997. He is currently a Professor with the School of Electronic Engineering and Optoelectronic Technology, Nanjing University of Science and Technology, where he is also an Associate Director with the Ministerial Key Laboratory of JGMT. He has authored or coauthored over 300 journal articles and conference papers, and has submitted over 30 patent applications.

His current research interests include microwave and millimeter-wave theories and technologies, microwave and millimeter-wave detection, and multimode compound detection.

Dr. Wu is a six-time recipient of ministerial and provincial-level science and technology awards.